

# RSC Applied Interfaces

Accepted Manuscript

This article can be cited before page numbers have been issued, to do this please use: E. Ghasemy, A. C. Tavares and K. K. Ghuman, *RSC Appl. Interfaces*, 2025, DOI: 10.1039/D5LF00195A.



This is an Accepted Manuscript, which has been through the Royal Society of Chemistry peer review process and has been accepted for publication.

Accepted Manuscripts are published online shortly after acceptance, before technical editing, formatting and proof reading. Using this free service, authors can make their results available to the community, in citable form, before we publish the edited article. We will replace this Accepted Manuscript with the edited and formatted Advance Article as soon as it is available.

You can find more information about Accepted Manuscripts in the [Information for Authors](#).

Please note that technical editing may introduce minor changes to the text and/or graphics, which may alter content. The journal's standard [Terms & Conditions](#) and the [Ethical guidelines](#) still apply. In no event shall the Royal Society of Chemistry be held responsible for any errors or omissions in this Accepted Manuscript or any consequences arising from the use of any information it contains.

## ARTICLE

Received 00th January 20xx,

**Facet- and Graphene-Support-Dependent Activity of Ta<sub>2</sub>O<sub>5</sub> for Oxygen Evolution Reaction**

Accepted 00th January 20xx

Ebrahim Ghasemy<sup>a</sup>, Ana C. Tavares<sup>\*,a</sup>, Kulbir K. Ghuman<sup>\*,a</sup>

DOI: 10.1039/x0xx00000x

**Abstract**

Ta<sub>2</sub>O<sub>5</sub> is among the few metal oxides that are stable in acidic media but, due to its insulating nature, its use in electrocatalytic oxygen evolution reaction (OER) has been less explored. Herein, density functional theory calculations were performed on three different Ta<sub>2</sub>O<sub>5</sub> facets, pristine and with O or Ta defects. The goal was to identify strategies to improve the OER performance of Ta<sub>2</sub>O<sub>5</sub> by establishing correlations with its intrinsic properties. The study revealed that the OER activity of Ta<sub>2</sub>O<sub>5</sub> is facet-dependent according to the following trend (200) > (120) > (001), which correlated with the Ta density on the topmost atomic layer. The lowest overpotential, 0.61 V, was observed at the Ta-O site of the pristine (200) facet, followed by a Ta site on the same facet with a Ta defect (0.63 V). The moderate density of states (DOS) at the Fermi level and lower Ta site density on the (200) surface contributed to its higher performance compared to other facets. The correlation analysis conducted by considering Bader charge, d-band analysis of Ta sites, and valence electrons showed strong correlations for (120) surfaces, whereas (200) surfaces had moderate correlations. As a conductive phase is often added to insulating materials in experiments, the (200) Ta<sub>2</sub>O<sub>5</sub>/graphene heterostructure was also studied. An overpotential as low as 0.39 V was found for the Ta-O sites of the heterostructure. According to the partial DOS analysis, the improved OER performance of the heterostructure can be attributed to the shift in the *d* orbitals of Ta sites toward lower energies and the increase in the DOS intensity. This study offers valuable insights for designing Ta<sub>2</sub>O<sub>5</sub>-based electrocatalysts for OER in acidic media.

**1. Introduction**

As a carbon-free energy vector, green hydrogen can enable clean electricity production, helping to meet the targets for reducing the emission of greenhouse gases (GHGs)<sup>1</sup>. It has been estimated that green hydrogen can reduce CO<sub>2</sub> emissions by six gigatonnes and meet 18% of energy demands<sup>2,3</sup>. According to the hydrogen strategy for Canada, clean hydrogen is capable of delivering 30% of end-use energy in the country by 2050, reducing the emission of CO<sub>2</sub> by up to 190 Mt<sup>4</sup>. When powered by electricity from renewable sources, water electrolyzers can sustainably produce green hydrogen<sup>5</sup>. This process involves two reactions, i.e., hydrogen evolution reaction (HER) and oxygen evolution reaction (OER) on the cathode and anode, respectively. However, the hydrogen production cost through hydrolysis (considering electricity cost of 5 cents US\$/kWh) is twice the H<sub>2</sub> production

methods based on natural gas<sup>6</sup>.

OER is a sluggish reaction that includes four electron-proton transfer steps and requires a high overpotential<sup>7-10</sup>. Proton exchange membrane water electrolyzers (PEMWEs) that work in an acidic environment are superior to alkaline electrolysis technologies. This is because PEMWEs have higher efficiency, higher production rates per unit electrode area, faster electrode kinetics, and a more compact design<sup>11</sup>. The best OER electrocatalysts are based on Ru and Ir materials, with Ru-based materials having higher OER activity but weaker stability compared to Ir-based materials<sup>12</sup>. The high cost and scarcity of these catalysts increase the economic risks of water electrolyzers. These risks can be minimized by developing precious metal-free catalysts and by diversifying catalyst material supply<sup>13</sup>. One strategy to develop electrocatalysts for corrosive acidic environments is to select materials with good inherent acidic stability and then tune their catalytic activity by modifying their structure. Among several transition metals, Tantalum-based materials are known for their good stability under acidic media<sup>14</sup>. However, tantalum oxides, the most-studied Ta-based materials, are insulators in their pristine form with poor or no OER performance<sup>15,16</sup>.

<sup>a</sup> Institut National de la Recherche Scientifique - Centre Énergie Matériaux Télécommunications, 1650 Boul. Lionel-Boulet, Varennes J3X 1P7, Quebec, Canada.



Several efforts have been made to induce electrical conductivity and improve the OER performance of Ta<sub>2</sub>O<sub>5</sub>-based electrocatalysts in alkaline media. Using the pulsed laser deposition method, Xiao et al.<sup>16</sup> grew stable Ta<sub>2</sub>O<sub>5</sub> nanolayers over a carbon cloth by controlling the oxygen environment. The pristine Ta<sub>2</sub>O<sub>5</sub> did not have catalytic activity, but the O-rich Ta<sub>2</sub>O<sub>5</sub> with a thickness of 8 nm showed an overpotential of 0.385 V at 10 mA/cm<sup>2</sup> in a 1 M KOH solution<sup>16</sup>. They reported that controlling the oxygen partial pressure and keeping the thickness of the nanolayer small could enable the efficient performance of Ta<sub>2</sub>O<sub>5</sub> for OER. Liu et al. synthesized Fe-doped O-rich Ta<sub>2</sub>O<sub>5</sub> nanolayers with a thickness of about 5 nm, which showed an overpotential of 0.38 V at 10 mA/cm<sup>2</sup> in the 1 M KOH solution with the optimal Fe concentration of 5 at.%<sup>15</sup>. This work reported that doping with transition metals could increase the electrical conductivity of Ta<sub>2</sub>O<sub>5</sub> and activate its surface for OER.

Yue et al. synthesized tantalum dioxyfluoride (TaO<sub>2</sub>F) over graphitized carbon<sup>17</sup>. When TaO<sub>2</sub>F was loaded over the carbon material with high electrical conductivity, an improvement in the charge transfer and OER performance was observed. The authors suggested that when fluorine was introduced into the TaO<sub>2</sub>F structure, more positive charge could be distributed by Ta sites of TaO<sub>2</sub>F compared to Ta<sub>2</sub>O<sub>5</sub>/CC (Cabot Vulcan XC 72R), Ta<sub>2</sub>O<sub>5</sub>, and KTaO<sub>3</sub>, which benefited the adsorption and reaction of intermediates. So, TaO<sub>2</sub>F loaded on graphitized carbon reached an overpotential of 0.360 V at 10 mA/cm<sup>2</sup> in the alkaline medium<sup>17</sup>. Ruiz-Cornejo et al.<sup>18</sup> supported Ta<sub>2</sub>O<sub>5</sub> over highly graphitic carbon nanofibers (CNFs), in which the sample with the lowest O/Ta (non-stoichiometric composition) led to the best OER performance in the alkaline medium. Ahmed et al.<sup>19</sup> loaded Ta<sub>2</sub>O<sub>5</sub> particles over Fe<sub>2</sub>O<sub>3</sub> through the hydrothermal treatment. They reported that the Fe<sub>2</sub>O<sub>3</sub>/Ta<sub>2</sub>O<sub>5</sub> double oxide heterostructure had a low overpotential

of 0.231 V in alkaline media, which was attributed to the synergistic effect and interfacial interaction between Fe<sub>2</sub>O<sub>3</sub> and Ta<sub>2</sub>O<sub>5</sub>. Ta<sub>2</sub>O<sub>5</sub> is stable under OER polarization conditions in acidic media<sup>20</sup>, yet there have been very few studies that have explored its performance under such an environment. Mondschein et al.<sup>14</sup> fabricated polycrystalline pellets of Ni<sub>2</sub>Ta through arc melting and molding. This material could combine the corrosion resistance of Ta and the OER activity of Ni in acidic media and achieve an overpotential of 0.570 V in 0.5 M H<sub>2</sub>SO<sub>4</sub>.

To develop stable and active Ta<sub>2</sub>O<sub>5</sub>-based electrocatalysts for OER in an acidic medium, it is crucial to identify strategies to enhance its performance and establish clear structure-property relationships. For instance, there have been inconsistent reports in the literature regarding the role of the O/Ta ratio in alkaline medium. Xiao et al.<sup>16</sup> reported better OER performance with O-rich Ta<sub>2</sub>O<sub>5</sub>, and Ruiz-Cornejo et al.<sup>18</sup> found that a lower O/Ta ratio results in better performance. Furthermore, while the use of carbon-based materials to improve the charge transfer with Ta<sub>2</sub>O<sub>5</sub>-based and NiFe alloy nanoparticles<sup>21</sup> electrocatalysts has been explored, their role in altering the electronic and electrocatalytic properties of Ta<sub>2</sub>O<sub>5</sub> remains unexplored.

Herein, we performed density functional theory (DFT) calculations on (200), (120), and (100) Ta<sub>2</sub>O<sub>5</sub> facets to identify strategies to unlock the OER performance of the Ta<sub>2</sub>O<sub>5</sub> in an acidic medium. The effect of a Ta or O defect on the electronic properties of (200) and (120) facets was studied, and thirty-five different sites on facets with or without a defect were considered for OER activity evaluation. Then, correlations were identified between the OER performance and structural and electronic properties, such as Bader charge (BC), valence electrons, and DOS of Ta<sub>2</sub>O<sub>5</sub> surfaces. Finally, the effect of graphene on the electronic properties and OER

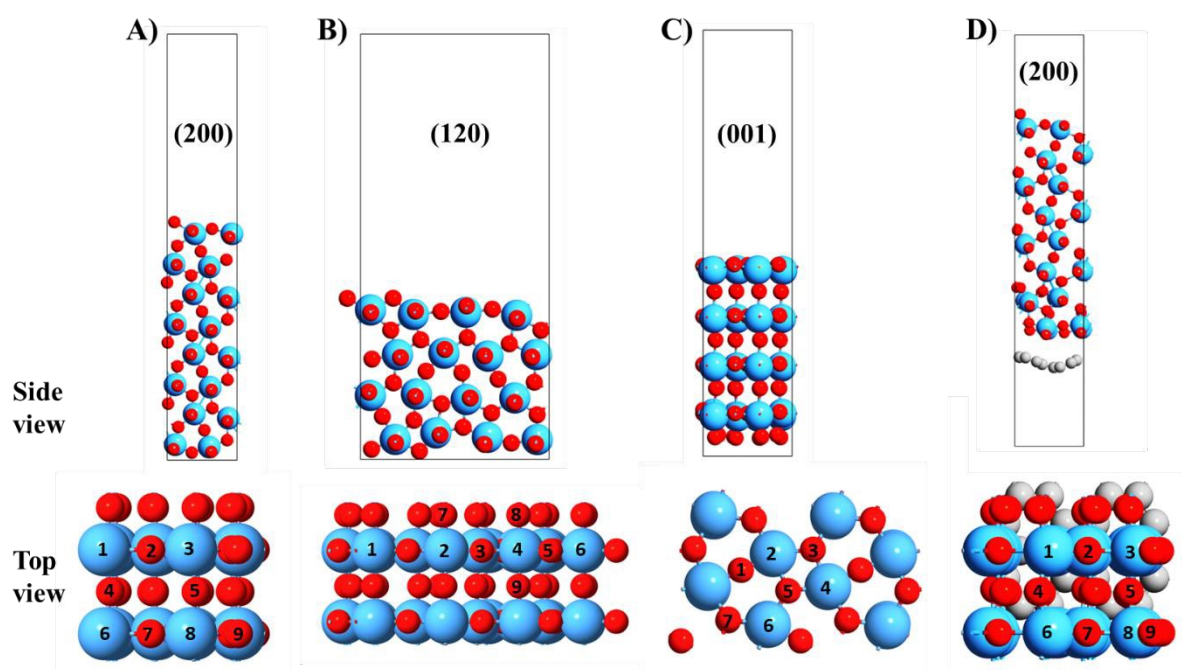


**Figure 1.** The side and top views of (A) (200), (B) (120), and (C) (001) Ta<sub>2</sub>O<sub>5</sub> facets, respectively. (D) The side and top views of the 200-Ta<sub>2</sub>O<sub>5</sub>/graphene model. The atoms with numbers in the lower panel represent the unique Ta and O sites on the surface. The O, Ta, and C atoms are represented by red, blue, and gray spheres, respectively.

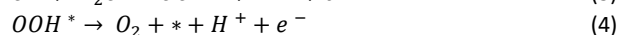
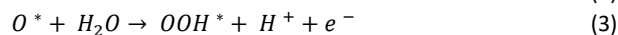
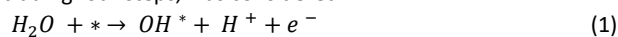


performance of the most active Ta<sub>2</sub>O<sub>5</sub> surface was investigated.

## 2. Computational Details

In this study, three Ta<sub>2</sub>O<sub>5</sub> facets, (200), (120), and (001), reported to be stable in DFT calculations<sup>16</sup> and experiments<sup>22</sup>, were examined, as illustrated in Figure 1 A-C. The orthorhombic λ-Ta<sub>2</sub>O<sub>5</sub> unit cell, with lattice parameters of *a* = 6.24 Å, *b* = 2×3.69 Å, and *c* = 3.82 Å, was used to model the surfaces<sup>23, 24</sup>. The 200-Ta<sub>2</sub>O<sub>5</sub>/graphene heterostructure was also modeled with the mean absolute strain of 2.94% for graphene and Ta<sub>2</sub>O<sub>5</sub>, Figure 1 D. The initial distance between (200) Ta<sub>2</sub>O<sub>5</sub> and graphene was changed between 2 to 5 Å to find the most stable heterostructure. As shown in Figure S1, the model created using the initial distance of 3 Å (final distance of 3.3 Å) had the lowest total energy and was the most stable, which was considered for OER performance evaluation. To avoid interactions between periodic images, all slab models were made with a vacuum greater than 15 Å. Spin-polarized DFT calculations were performed using the Perdew–Burke–Ernzerhof (PBE) exchange-correlation functional in the generalized gradient approximation (GGA). All the DFT calculations were conducted using the Quantum Espresso software<sup>25</sup>. Furthermore, we utilized the DFT-D3 correction method in Grimme's scheme<sup>26, 27</sup> for a more accurate description of the long-range van der Waals (vdW) interactions. The kinetic energy cut-off values of 35 and 350 Ry were used for wavefunctions and charge density, respectively. The energy threshold was set to 10<sup>-4</sup> Ry for the self-consistent field (SCF) convergence. Davidson iterative diagonalization was employed to relax each system (without variable size) until the residual Hellman–Feynman force magnitude on each atom reached below the 10<sup>-3</sup> Ry Bohr<sup>-1</sup>. The DFT+U was performed to reach more accurate electronic properties. The U value of 3.66 V was taken from the Materials Project database<sup>28, 29</sup>, as it has been used for developing Ta-based electrocatalysts in the literature<sup>30</sup>. The k-point sampling of 2 × 2 × 1 was used to relax the structures, and the k-point samplings of 4 × 4 × 1 and 6 × 6 × 1 were adopted for the SCF and non-self-consistent field (nSCF) calculations, respectively, to calculate the DOS and partial DOS (PDOS). The BC analysis was performed to assess the electron density of each surface<sup>31</sup>.

The OER performance was investigated by calculating the theoretical OER overpotential ( $\eta$ ) according to the computational hydrogen electrode (CHE)<sup>32</sup>. The reaction mechanism is shown in Equations 1-4. The following associative reaction mechanism, including four steps, was considered:



where, \* indicates the surface, and O\*, OH\*, and OOH\* refer to the adsorbed intermediates. To calculate the adsorption energy ( $\Delta E$ ) of each intermediate, Equations 5-7 were used:

$$\Delta E_{O^*} = E(O^*) - E(*) - [E(H_2O_{(g)}) - E(H_{2(g)})] \quad (5)$$

$$\Delta E_{OH^*} = E(OH^*) - E(*) - [E(H_2O_{(g)}) - 0.5 E(H_{2(g)})] \quad (6)$$

$$\Delta E_{OOH^*} = E(OOH^*) - E(*) - [2 E(H_2O_{(g)}) - 1.5 E(H_{2(g)})] \quad (7)$$

in these equations,  $E(*)$ ,  $E(O^*)$ ,  $E(OH^*)$ , and  $E(OOH^*)$  are the total energy of the surface without adsorbates and with adsorbed intermediates of O\*, OH\*, and OOH\*, respectively. After finding the adsorption  $\Delta E$  of each intermediate, adsorption free energies ( $\Delta G_{\text{adsorption}}$ ) were calculated according to Equation (8):

$$\Delta G_{\text{adsorption}} = \Delta E_{\text{adsorption}} + \Delta G_{\text{correction}} \quad (8)$$

For O\*, OH\*, and OOH\*,  $\Delta G_{\text{correction}}$  values (which include the contributions of zero-point energy, integrated heat capacity from 0 to 298.15 K, and entropy) of 0.044, 0.295, and 0.377 eV were used, respectively<sup>32</sup>. Finally, Gibbs free energy ( $\Delta G_{\text{Step 1-4}}$ ) of each step at  $U=0$  V and OER overpotential ( $\eta$ ) were calculated according to Equations 9-13:

$$\Delta G_{\text{Step 1}} = \Delta G_{OH^*} - \Delta G(H_2O) = \Delta G_{OH^*} - 0 = \Delta G_{OH^*} \quad (9)$$

$$\Delta G_{\text{Step 2}} = \Delta G_{O^*} - \Delta G_{OH^*} \quad (10)$$

$$\Delta G_{\text{Step 3}} = \Delta G_{OOH^*} - \Delta G_{O^*} \quad (11)$$

$$\Delta G_{\text{Step 4}} = \Delta G_{O_2} - \Delta G_{OOH^*} = 4.92 - \Delta G_{OOH^*} \quad (12)$$

$$\eta = \max[\Delta G_{\text{Step 1}}; \Delta G_{\text{Step 2}}; \Delta G_{\text{Step 3}}; \Delta G_{\text{Step 4}}] / e - 1.23 \text{ V} \quad (13)$$

## 3. Results and discussion

### 3.1. OER performance of pristine and defected Ta<sub>2</sub>O<sub>5</sub> surfaces

First, we investigated the OER performance of various sites on pristine and defected Ta<sub>2</sub>O<sub>5</sub> facets. Specifically, (200), (120), and (001) facets were investigated as they were experimentally observed and were proved to be stabilized in DFT calculations<sup>16</sup>. Additionally, on (200) and (120) facets, O or Ta were removed to create defected surfaces. More precisely, O5d-200-Ta<sub>2</sub>O<sub>5</sub>, O7d-200-Ta<sub>2</sub>O<sub>5</sub>, O9d-200-Ta<sub>2</sub>O<sub>5</sub>, Ta1d-200-Ta<sub>2</sub>O<sub>5</sub>, and Ta3d-200-Ta<sub>2</sub>O<sub>5</sub> surfaces were modeled by removing O5, O7, O9, Ta1, and Ta3 atoms, respectively, from the pristine (200) surface (Figure 1A). In this nomenclature, "d" indicates surfaces with an O or Ta defect. Similarly, the O5d-120-Ta<sub>2</sub>O<sub>5</sub>, O9d-120-Ta<sub>2</sub>O<sub>5</sub>, Ta4d-120-Ta<sub>2</sub>O<sub>5</sub>, and Ta6d-120-Ta<sub>2</sub>O<sub>5</sub> surfaces were modeled by removing O5, O9, Ta4, and Ta6, respectively, from the pristine (120) surface (Figure 1B).

The OER performance of (200) and (120) surfaces with and without defects and the pristine (001) surface is detailed in Tables S1-3, including the  $\Delta G$  values for adsorption of reaction intermediates and Steps 1-4 (Equations 9-12). The defects on the (001) facet were not investigated because the pristine (001) surface showed larger overpotentials, as summarised in the SI, compared to the (200) and (120) surfaces. Figure 2 illustrates the OER reaction pathway for Ta or Ta-O sites with overpotentials below 0.7 V.

On the pristine (200) surface, Step 2 (OH\* to O\*) was the rate-limiting step on the Ta8-O5 bridge site, and Step 3 (O\* to OOH\*) was the rate-limiting step on the two Ta sites (Table S1). The lowest overpotential, 0.61 V, was found on the Ta8-O5 bridge site, as illustrated in Figure 2 A. Creating oxygen defects increased the  $\Delta G_{\text{Step 4}}$  on the O7d-, O5d-, and O9d-200-Ta<sub>2</sub>O<sub>5</sub> surfaces, making oxygen desorption difficult. Therefore, Step 4 became rate limiting on most sites of oxygen-deficient (200) surface. In contrast, the Ta1 site on the Ta3d-200-Ta<sub>2</sub>O<sub>5</sub> surface had the lowest overpotential of 0.63 V (Step 3), outperforming other single Ta sites on both pristine and O/Ta-defected surfaces.





On pristine (120), Step 2 or Step 3 was the rate-limiting step for Ta and Ta-O bridge sites, and the lowest overpotential was found on the Ta1 site (0.68 V, Figure 2 B). Oxygen defects in O5d- and O9d-120-Ta<sub>2</sub>O<sub>5</sub> surfaces increased the  $\Delta G_{\text{Step4}}$ , deteriorating the OER performance (Table S2). An overpotential of 0.76 V was found for the Ta2 site on the Ta6d-120-Ta<sub>2</sub>O<sub>5</sub> surface, which compared favorably with respect to the similar site on the pristine (120) facet (1.03 V) and the Ta4d-120-Ta<sub>2</sub>O<sub>5</sub> (1.22 V) surfaces.

The pristine (001) surface had the poorest performance (overpotentials above 1.8 V) compared to both (120) and (200) surfaces. On this surface, the conversion of O\* to OOH\* (step 3) limited the reaction (Table S3).

### 3.2. OER performance of 200-Ta<sub>2</sub>O<sub>5</sub>/graphene heterostructure

In practical applications, a conductive phase is added to insulating electrocatalysts to facilitate electron transport through the electrode<sup>16-18, 33</sup>; hence, we modeled a Ta<sub>2</sub>O<sub>5</sub>/graphene heterostructure and investigated its OER performance. The (200) surface was considered for this heterostructure, Figure 1 D, as it showed the highest OER activity. One Ta site and three Ta-O bridge

sites were investigated. The OER performance parameters ( $\Delta G_{\text{Step1-4}}$ ,  $\Delta G$  of reaction intermediates (OH\*, O\*, and OOH\*)) and overpotential of different sites on 200-Ta<sub>2</sub>O<sub>5</sub>/graphene heterostructure are summarized in Table S4. Figure 3 A presents the energy diagrams for Ta6-O7 and Ta6 sites, the best-performing ones with an overpotential of 0.39 and 0.45 V, respectively. The energy diagram of the Ta6 site of 200-Ta<sub>2</sub>O<sub>5</sub>/graphene and of pristine (200) are further compared in Figure 3 B. As indicated in the figure, the overpotential of 1.07 V on the pristine surface decreased significantly to 0.45 V on the heterostructure. This is similar to our previous study, where adding graphene decreased the OER overpotential of Nb<sub>2</sub>C MXene<sup>34</sup>.

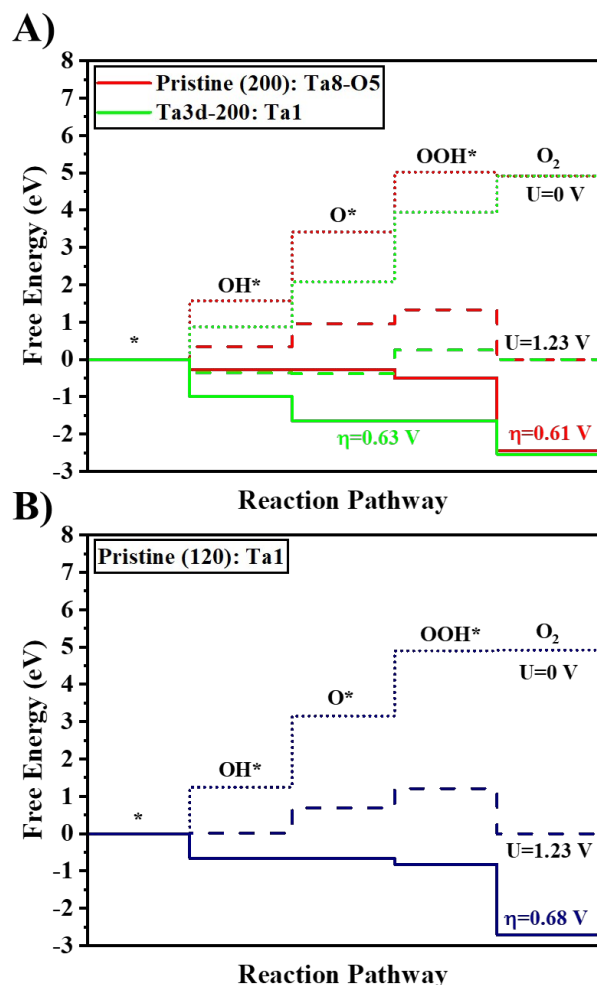


**Figure 2.** Free energy diagrams for A) the Ta8-O5 bridge on the pristine (200) surface, the Ta1 site on the Ta3d-200-Ta<sub>2</sub>O<sub>5</sub> surface, and B) the Ta1 site on the pristine (120) surface. The dotted, dashed, and straight lines indicate the free energy diagrams at potentials of 0, 1.23 V, and the overpotential at which OER becomes downward, respectively.

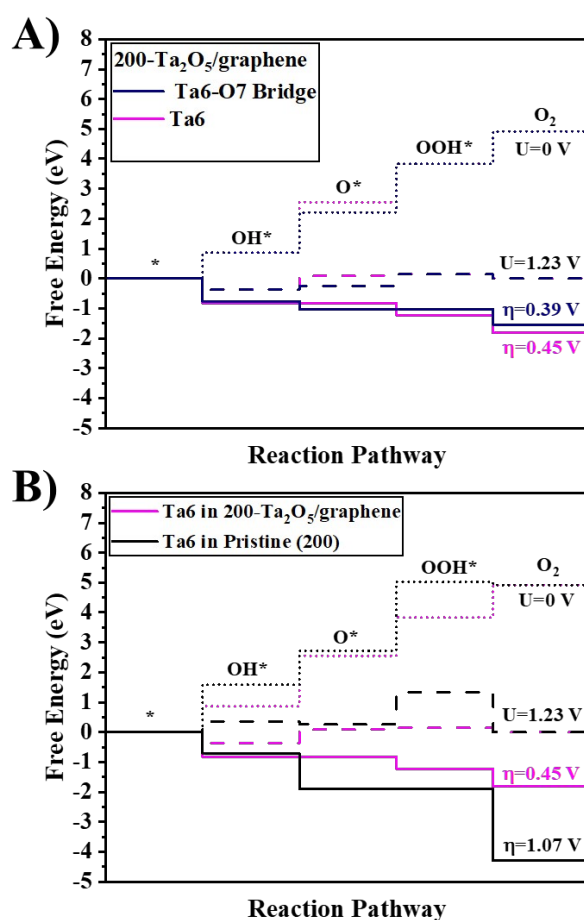


**Figure 3.** A) The reaction pathway Ta6-O7 and Ta6 sites on 200-Ta<sub>2</sub>O<sub>5</sub>/graphene. B) Comparing the reaction pathway of the Ta6 site on 200-Ta<sub>2</sub>O<sub>5</sub>/graphene and pristine (200) Ta<sub>2</sub>O<sub>5</sub>. The dotted, dashed, and straight lines indicate the free energy diagrams at potentials of 0, 1.23 V, and the overpotential at which OER becomes downward, respectively.



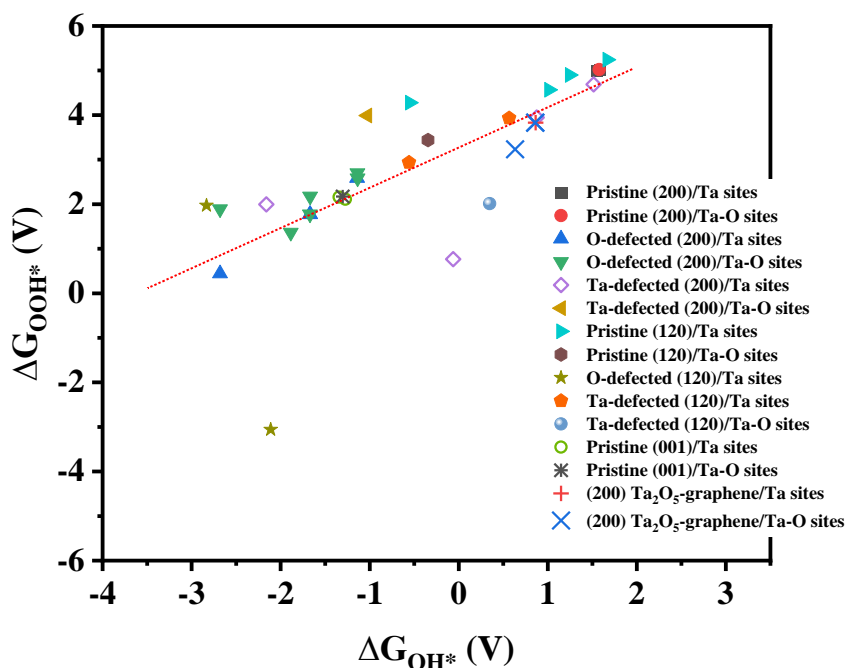


**Figure 4.** Scaling relationships of adsorption  $\Delta G$  of  $\text{OOH}^*$  vs.  $\text{OH}^*$  for all Ta and Ta-O sites on all facets with or without a defect.

The scaling relationship for  $\Delta G_{\text{OOH}^*}$  vs.  $\Delta G_{\text{OH}^*}$  is plotted in Figure 4, showing a linear correlation for most sites. According to the figure, some sites, including Ta sites on O-defected (120) and O-defected (200) surfaces, exhibited strong adsorption of intermediates, which increased the overpotential, as presented in Tables S1 and S2. In contrast, the intermediates were weakly adsorbed on some sites, such as Ta sites of pristine (120) and pristine (200). Since 200- $\text{Ta}_2\text{O}_5/\text{graphene}$  heterostructure showed the lowest overpotential, it can be stated that it possessed comparatively optimum adsorption  $\Delta G$  of  $\text{OOH}^*$  and  $\text{OH}^*$ . This figure showed  $\Delta G_{\text{OOH}^*} = (0.90715 \pm 0.13051)\Delta G_{\text{OH}^*} + (3.29035 \pm 0.1922)$ , which is close to the

reports in the literature<sup>32, 35</sup>. The nearly linear relationship, with a slope close to 1, indicates that  $\text{OOH}^*$  and  $\text{OH}^*$  bind to the surface in a similar, single-bonded adsorption mode<sup>36, 37</sup>.

### 3.3. Analysis of $\text{Ta}_2\text{O}_5$ facets with or without a defect

This section deciphers the reasons behind the distinct performances of the facets. Since the geometry of different facets can affect the electrocatalytic performance<sup>38</sup>, the compactness of each pristine facet was analyzed, as explained in SI. The surface compactness of the (001) and (200) facets (the topmost atoms) is  $0.21 \text{ atom}/\text{\AA}^2$ , and that of the (120) surface is  $0.23 \text{ atom}/\text{\AA}^2$ . Moreover, the density of Ta atoms on the layers of the (001), (120), and (200) facets is 0.087, 0.072, and 0.071 Ta atoms/ $\text{\AA}^2$ , respectively. Thus, the trend of OER

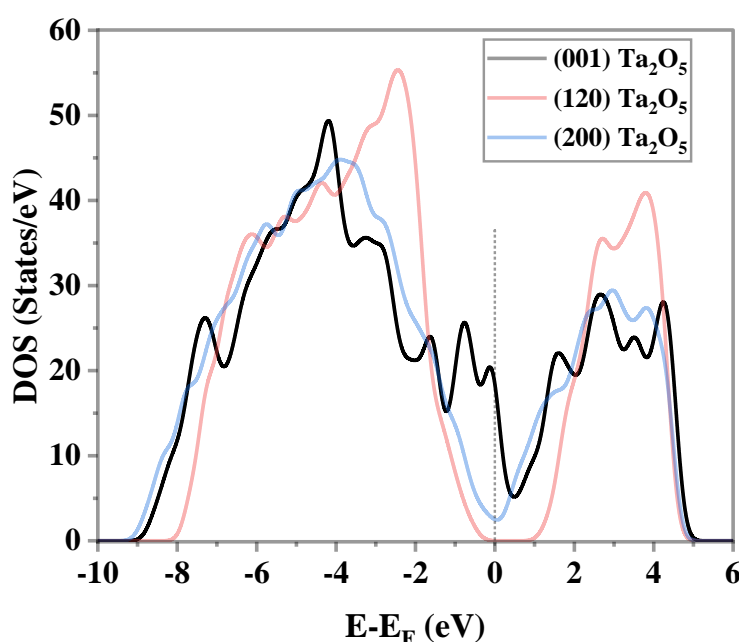


**Figure 5.** Comparing the DOS curves of pristine (001), (120), and (200) surfaces.



performance for these surfaces followed the Ta density on the facets: the (001) facet with the highest Ta density shows the highest overpotentials (between 1.8 and 3.5 V, Table S3). Instead, on the other facets with lower Ta density, the overpotentials were below 1.1 V for the pristine (200) (Table S1) and between 0.68 and 2.0 V for most sites (except one with 2.6 V, Table S2) on the pristine (120) facet. This result is similar to RuO<sub>2</sub>, where the (111) facet with the lowest active site density had the lowest overpotential of 0.35 V, and the (101) facet with the highest active site density had the highest overpotential of 0.60 V<sup>39</sup>.

Figure 5 compares the DOS curves of the pristine facets. It shows that the (001) and (200) facets do not have a bandgap, but the former has higher DOS at the Fermi level compared to the latter. Instead, the (120) facet has a band gap, indicating an insulating behavior. The Fermi-level electrons can increase the likelihood of electron transfer to reaction intermediates<sup>40, 41</sup>. In the (200) facet, the DOS at the Fermi level was intermediate between the (001) and (120) facets, which may explain its better OER performance. This balance enables the optimal electronic contribution to the intermediates - neither too high (strongly adsorbing intermediates) nor too low (weakly adsorbing intermediates) - that can facilitate the efficient bonding and electron transfer between the surface and intermediates.

The total DOS analysis of (120) surfaces without and with Ta or O defects are compared in Figure S2 A. In the pristine (120), the Fermi level is closer to the valence band (VB) edge. In O5d- and O9d-120-Ta<sub>2</sub>O<sub>5</sub> surfaces, creating O defects shifted the VB states away from the Fermi level and placed the Fermi level in the conduction band (CB). This shows the formation of the n-type semiconductor. In contrast, creating Ta defects, as in Ta6d- and Ta4d-120-Ta<sub>2</sub>O<sub>5</sub>, shifted the Fermi level into the VB states, indicating the formation of a p-type semiconductor<sup>42</sup>.

The total DOS analysis of the (200) surface with and without defects is shown in Figure S3 A. Creating Ta defects on this surface did not introduce a bandgap, keeping its metallic nature. In the (200) surface with the Ta defect, the Fermi level was located inside the VB. However, the O defects created a bandgap and shifted the Fermi level inside the CB, exhibiting n-type semiconductor behavior. This trend was similar to the (120) facet with a Ta or O defect. This is significant because reducing the (200) surface may lead to a decrease in the electrical conductivity.

### 3.4. Analysis of the varied OER performance of different Ta sites

In addition to the electronic and geometrical analysis of the pristine and defective facets, all unique Ta sites were screened individually. To this end, the PDOS curves of (120) and (200) facets were plotted, and the *d* orbitals of each Ta site were compared since they can significantly affect the catalytic activity<sup>43-45</sup>. Then, the PDOS width at the Fermi level, the maximum PDOS width in the valence band (MPWV) and its position<sup>46</sup>, maximum PDOS width in the conduction band (MPWC) and its position, valence band maxima (VBM), and conduction band minima (CBM) of the *d* orbitals were

extracted. The schematic representation of parameters derived from *d* orbitals of single Ta sites is shown in Figure S5. Moreover, the BC of the Ta sites and the nearest atom, and the sum of valence electrons (SVE) within 2 and 3 Å radii were calculated. Finally, heatmaps for (120) and (200) surfaces are provided in Figures 6 and 8, respectively, to highlight possible correlations between the OER performance ( $\Delta G_{\text{Steps 1-4}}$ ,  $\Delta G_{\text{OH}^*}$ ,  $\Delta G_{\text{O}^*}$ ,  $\Delta G_{\text{OOH}^*}$ , overpotential) and the properties of each Ta site.

#### 3.4.1. Properties of Ta sites on the (120) Ta<sub>2</sub>O<sub>5</sub> surface

The PDOS analysis of *d* orbitals of the Ta sites on the (120) surface with and without defects is shown in Figure S2 B. As expected, the same trends as with the total DOS analysis were found: creating O or Ta defects shifted the Fermi level to inside the CB and VB, respectively. The heatmap in Figure 6 shows the interdependence between properties of each Ta site (data derived from *d* orbitals, BC, and SVE within the radii of 2 and 3 Å) with OER performance metrics for this surface, which was calculated using Pearson's correlation coefficient analysis<sup>47</sup>. Notably, heatmaps show the relationship between different parameters, and they cannot be extended to features and data that are not included in our calculations.

Significant correlations were found between the properties of Ta *d* orbitals and OER performance metrics. MPWV showed strong correlations with  $\Delta G_{\text{Step 2}}$ ,  $\Delta G_{\text{Step 4}}$ ,  $\Delta G_{\text{O}^*}$ , and  $\Delta G_{\text{OOH}^*}$ , with its position also playing a significant role, as seen in Figures 6 and 7. The higher the MPWV, the higher the contribution of valence electrons to the reaction, and its position can control the hybridization between reaction intermediates and the active site. An increase in the MPWV could decrease  $\Delta G_{\text{Step 2}}$  and increase  $\Delta G_{\text{Step 4}}$ , suggesting that a higher electron presence might hinder the oxygen desorption step. The MPWV position had a correlation of -0.74 with  $\Delta G_{\text{Step 4}}$ , indicating that shifting the MPWV closer to the Fermi level can decrease  $\Delta G_{\text{Step 4}}$ , thereby facilitating the oxygen desorption step. In addition, MPWV had the strongest correlation (0.88) with overpotential. The heatmap also reveals that MPWC and its position had moderate correlations with OER performance metrics. Interestingly,  $\Delta G_{\text{Step 3}}$  (O\* to OOH\*) only correlated with the PDOS width at the Fermi level, 0.73, showing that the increase in Fermi-level electrons can increase  $\Delta G_{\text{Step 3}}$ . The role of DOS width at the Fermi level in OER has been observed in the literature<sup>48</sup>, where the increase in the DOS at the Fermi level decreased the adsorption energy gap between O\* and OOH\*<sup>48</sup>.



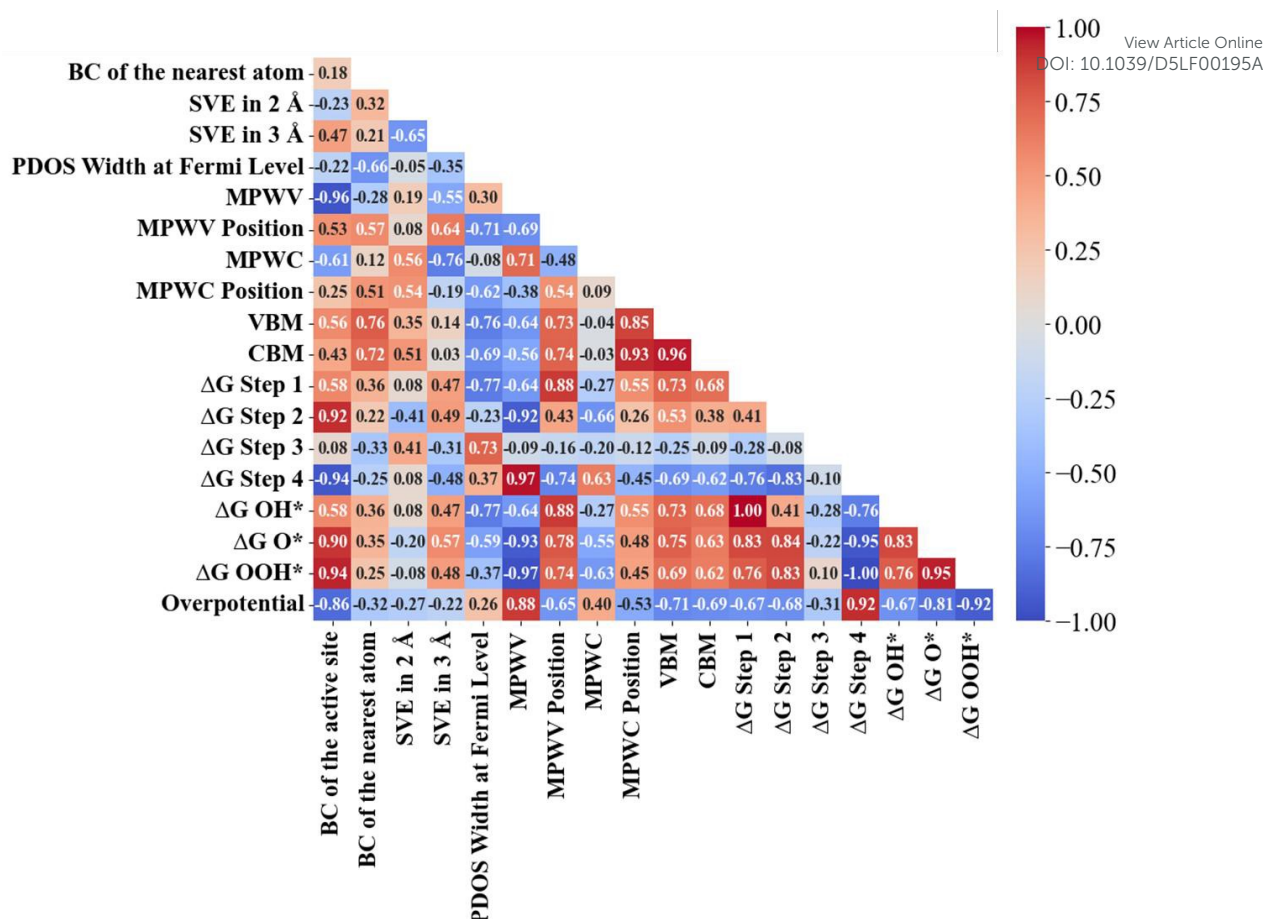


**Figure 6.** Correlations between the OER performance metrics ( $\Delta G_{\text{Step 1-4}}$ ,  $\Delta G_{\text{OH}^*}$ ,  $\Delta G_{\text{O}^*}$ ,  $\Delta G_{\text{OOH}^*}$ , and overpotential) and Bader charge (BC) of the active site and its nearest neighboring atom, the sum of valence electrons (SVE) within 2 and 3 Å radii, the PDOS width at Fermi level, the maximum PDOS width in the valence band (MPWV) and its position, maximum PDOS width in the conduction band (MPWC) and its position, the valence band maxima (VBM), and conduction band minima (CBM) for Ta sites on the (120) facet with and without defects.

The BC of Ta sites (Figures 6 and 7 B) strongly correlated with  $\Delta G_{\text{O}^*}$  and  $\Delta G_{\text{OOH}^*}$ , and with  $\Delta G_{\text{Step 2}}$  and  $\Delta G_{\text{Step 4}}$ . Notably, while increasing the BC increased  $\Delta G_{\text{O}^*}$  and  $\Delta G_{\text{Step 2}}$  ( $\text{OH}^*$  to  $\text{O}^*$ ), it simultaneously reduced  $\Delta G_{\text{Step 4}}$  (the oxygen desorption step). Therefore, a higher BC does not necessarily enhance OER performance. However, increasing the BC of Ta sites can improve the OER performance for sites where Step 4 is rate-

limiting. Moreover, a strong negative correlation of -0.86 was found between the BC of Ta atoms and the OER overpotential, which is in line with the literature showing the strong effect of BC on the OER activity of various materials<sup>49-52</sup>. The negative correlation suggests that a decrease in BC (i.e., lower positive charge on the Ta sites) leads to an increase in overpotential. It should be noted that BC of the nearest O atoms and SVE within 2 and 3 Å radii of Ta sites had no significant effect on

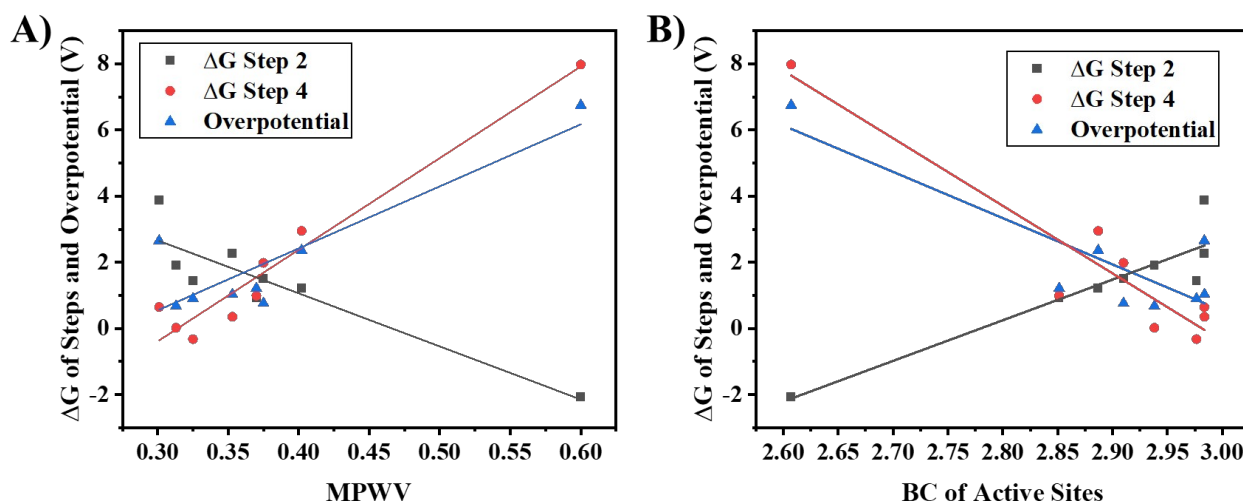


**Figure 7.** The relation between  $\Delta G_{\text{Steps 2\&4}}$  and overpotential and (A) MPWV and (B) BC of eight Ta sites for the (120) surfaces with and without defects.





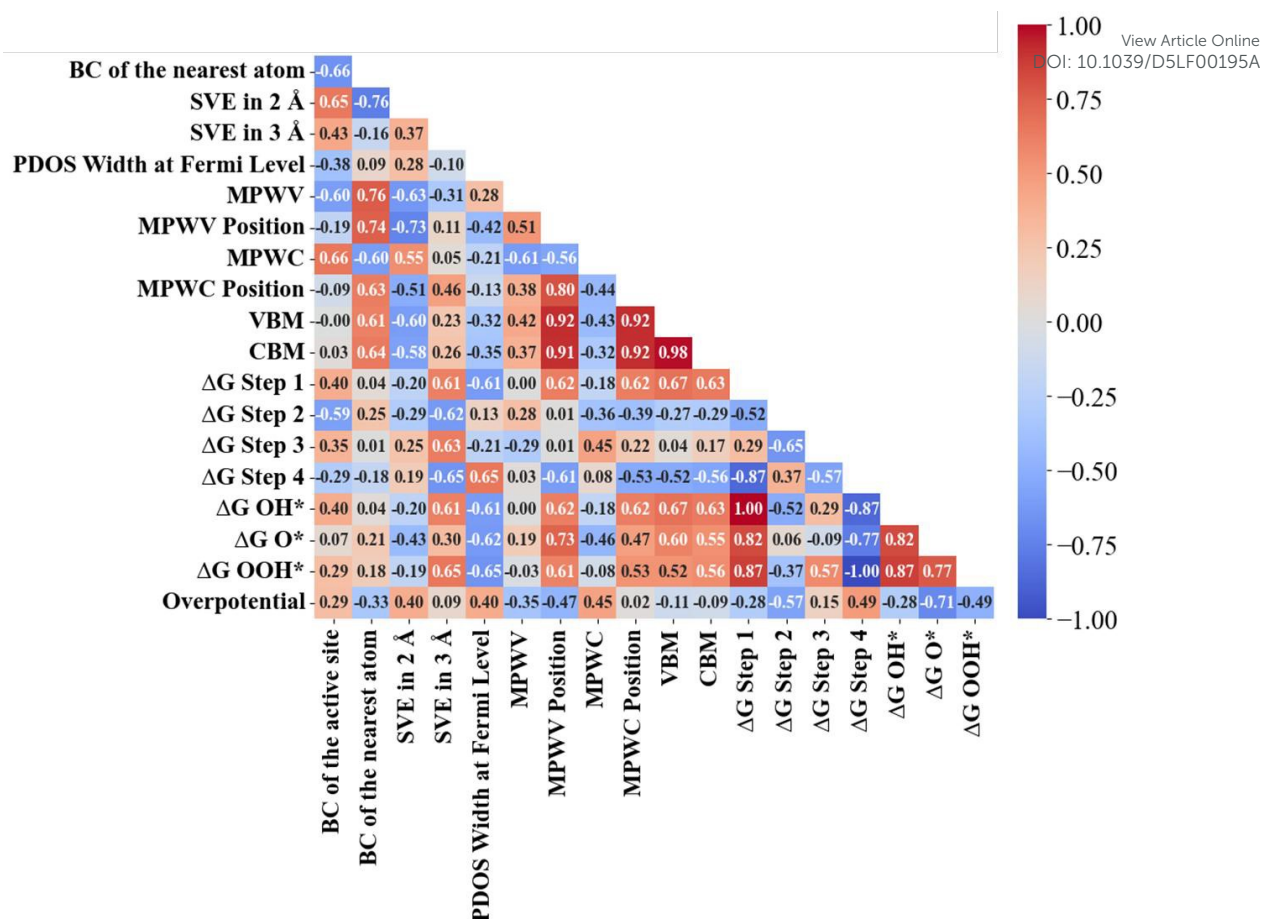


**Figure 8.** Correlations between the OER performance metrics ( $\Delta G_{\text{Step 1-4}}$ ,  $\Delta G_{\text{OH}^*}$ ,  $\Delta G_{\text{O}^*}$ ,  $\Delta G_{\text{OOH}^*}$ , and overpotential) and Bader charge (BC) of the active site and its nearest neighboring atom, the sum of valence electrons (SVE) within 2 and 3 Å radii, the PDOS width at Fermi level, the maximum PDOS width in the valence band (MPWV) and its position, maximum PDOS width in the conduction band (MPWC) and its position, the valence band maxima (VBM), and conduction band minima (CBM) for Ta sites on the (200) facet with and without defects.

the OER performance.

### 3.4.2. Properties of Ta sites on the (200) Ta<sub>2</sub>O<sub>5</sub> surface

The PDOS analysis of the Ta *d* orbitals of the (200) surface with and without a defect is shown in Figure S3 B. Similar to the (120) surfaces with O defects, the Fermi level was in the CB, and the reverse was found for structures having Ta defects. Moreover, as shown in Figure S3 B, the *d* orbital of Ta atoms on the pristine (200) facet did not significantly contribute to the PDOS at the Fermi level, where the *p* orbital of oxygen sites dominated.

The correlation heatmap of the (200) surface with and without defects is shown in Figure 8. In contrast to 120-Ta<sub>2</sub>O<sub>5</sub> surfaces, (200) surfaces did not have strong correlations with the properties of Ta sites. This again indicates a significant facet-dependent behavior of Ta<sub>2</sub>O<sub>5</sub> for OER, similar to other materials such as IrO<sub>2</sub> and Co-based electrocatalysts<sup>39, 53, 54</sup>.

A moderate correlation was observed between the BC and  $\Delta G_{\text{Step 2}}$  (-0.59) and between the SVE within a 3 Å radius and  $\Delta G_{\text{Step 1-4}}$ ,  $\Delta G_{\text{OH}^*}$ , and  $\Delta G_{\text{OOH}^*}$ . This suggests that the presence of valence electrons at a longer range (3 Å) is more influential in modulating the reaction than at a shorter range (2 Å). Moreover, the PDOS width at the Fermi level had correlations

of -0.61 to -0.65 with  $\Delta G_{\text{OH}^*}$ ,  $\Delta G_{\text{O}^*}$ , and  $\Delta G_{\text{OOH}^*}$ . This implies that a higher density of electrons at the Fermi level could decrease the  $\Delta G$  of all intermediates and increase  $\Delta G_{\text{Step 4}}$ . Similar results have been found<sup>55</sup>, for instance, between the adsorption energy of O<sub>2</sub> and DOS width at the Fermi level for N-doped graphdiyne<sup>56</sup>.

### 3.5. The 200-Ta<sub>2</sub>O<sub>5</sub>/graphene heterostructure

Here, the effect of graphene on the electronic properties and OER performance of the (200) Ta<sub>2</sub>O<sub>5</sub> facet is discussed. Figure 9 A compares the total DOS curves of 200-Ta<sub>2</sub>O<sub>5</sub>/graphene and (200) Ta<sub>2</sub>O<sub>5</sub>. The major difference is the higher intensity of the DOS curve in the VB and CB in the 200-Ta<sub>2</sub>O<sub>5</sub>/graphene structure, which can improve the orbital hybridization level between the surface and reaction intermediates. In addition, the DOS width at the Fermi level was reduced after adding graphene, which indicates the lower capability of the surface in transferring electrons to intermediates. To analyze this further, we compared the PDOS curve of O and C *p* orbitals and Ta *d* orbitals in the heterostructure and O *p* and Ta *d* orbitals in (200) Ta<sub>2</sub>O<sub>5</sub>, as shown in Figure 9 B. Regarding the O *p* orbitals, the PDOS intensity in the VB and CB was increased after adding graphene. However, the O *p* orbitals of the (200) surface contributed more at the Fermi level compared to that of the 200-Ta<sub>2</sub>O<sub>5</sub>/graphene heterostructure. The PDOS intensity of Ta *d*



orbitals in the VB and CB for the 200-Ta<sub>2</sub>O<sub>5</sub>/graphene was higher than that of the pristine (200) surface. This leads to higher valence electron contribution of Ta sites of 200-Ta<sub>2</sub>O<sub>5</sub>/graphene during the reaction (stronger hybridization), which might explain the better performance of Ta sites after adding graphene. In addition, the C *p* orbitals in the heterostructure overlapped with Ta *d* orbitals in the VB in the range of -8 to -4 eV.

Figure 9 C compares the PDOS curves of *d* orbitals of the Ta6 site over 200-Ta<sub>2</sub>O<sub>5</sub>/graphene and pristine (200). The MPWV and MPWC in the 200-Ta<sub>2</sub>O<sub>5</sub>/graphene were higher, and their position shifted toward lower energies. As a result, the Ta6

sites over pristine (200) and 200-Ta<sub>2</sub>O<sub>5</sub>/graphene surfaces had overpotentials of 0.91 and 0.46 V, respectively, where the rate-limiting step was Steps 3 and 2. This can be attributed to the higher PDOS intensity of the *d* orbital in the VB after adding graphene, which increased  $\Delta G_{\text{step 4}}$  from -0.08 to 1.09 V and decreased  $\Delta G_{\text{step 3}}$  from 2.14 to 1.28 V. Based on the results, it is clear that the changes in the intensity of *d* orbitals of Ta sites in heterostructure lead to significant differences in performances. Notably, an oxygen atom was close to Ta8 on the 200-Ta<sub>2</sub>O<sub>5</sub>/graphene surface, so we could not evaluate a single Ta8 site since the adsorbates were interacting with both Ta and O in this case.

#### 4. Conclusion

In this work, DFT calculations were performed on the (200), (120), and (001) surfaces of Ta<sub>2</sub>O<sub>5</sub> and on the 200-Ta<sub>2</sub>O<sub>5</sub>/graphene heterostructure to identify strategies to enhance the OER performance of Ta<sub>2</sub>O<sub>5</sub>. New insights into the OER activity of Ta sites on pristine facets were established. The (200) facet, with the lowest Ta site density and moderate DOS at the Fermi level, showed the lowest overpotential compared to the (120) and (001) facets. Creating Ta defects could decrease the overpotential of a Ta site on the (200) and (120) facets. However, creating O defects created a bandgap in the (200) facet and increased the overpotential on (200) and (120) facets. Correlation heatmaps were established between properties of each Ta site on the (200) and (120) facets and the OER performance metrics. On the second best-performing facet, the (120), the Bader charge and *d* orbitals of Ta sites at the VB significantly modulated the performance, correlating strongly with the Gibbs free energy ( $\Delta G$ ) of steps 1, 2, and 4. However, on the (200) facet, only SVE within 3 Å and PDOS width at the Fermi level exhibited moderate correlations. The 200-Ta<sub>2</sub>O<sub>5</sub>/graphene heterostructure showed a substantially low overpotential of 0.39 V on a Ta-O site. The PDOS analysis showed that the improved OER performance of the heterostructure was due to the shift of the *d* orbitals of Ta sites toward lower energies and the increase in the DOS intensity after adding graphene. Overall, the best strategies to unlock the potential of Ta oxide in OER is to synthesize a heterostructure formed by (200) Ta<sub>2</sub>O<sub>5</sub> and graphene, prevent the formation of the (001) facet, and/or create Ta defects in Ta<sub>2</sub>O<sub>5</sub> nanoparticles or thin films. If validated in experiments, these results would conduce to Ta<sub>2</sub>O<sub>5</sub>-based materials as promising non-precious OER electrocatalysts under acidic media.

#### Acknowledgments

The authors acknowledge the Natural Sciences and Engineering Research Council of Canada (NSERC) [Discovery grant program RGPIN-2020-05924; RGPIN-2020-05950, Alliance program [576728-2022], PRIMA Québec [R24-13-001-PME], Canada Research Chair (CRC) program, and the Canada Foundation for Innovation (CFI) for infrastructure and operating funds. This research was financed by enabled in part by support provided by Calcul Québec (<https://www.calculquebec.ca>) and Compute Canada ([www.computeCanada.ca](http://www.computeCanada.ca)). The authors would like to thank Niobay for their financial support.

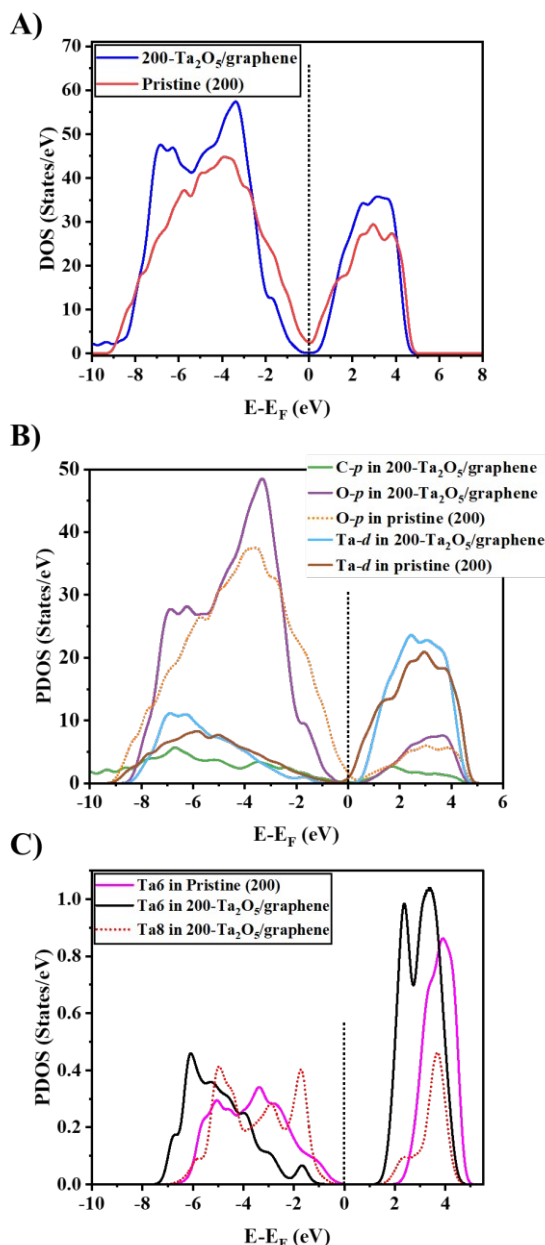


**Figure 9.** A) Comparing the DOS of 200-Ta<sub>2</sub>O<sub>5</sub>/graphene and pristine (200) Ta<sub>2</sub>O<sub>5</sub>. B) Comparing the PDOS analysis of C and O *p* orbitals and Ta *d* orbital of 200-Ta<sub>2</sub>O<sub>5</sub>/graphene and pristine (200) Ta<sub>2</sub>O<sub>5</sub>, respectively. C) PDOS analysis of the *d* orbital of the Ta6 site on 200-Ta<sub>2</sub>O<sub>5</sub>/graphene and pristine (200) Ta<sub>2</sub>O<sub>5</sub>. D) PDOS analysis of *p* and *d* orbitals of active O and Ta sites on 200-Ta<sub>2</sub>O<sub>5</sub>/graphene.



## Author Contributions

Ebrahim Ghasemy: Data Curation, Investigation, Methodology, Visualization, and Writing – original draft, and Writing – review & editing. Ana C. Tavares: Conceptualization, Project Administration, Supervision, Funding Acquisition, Writing – review & editing. Kulbir Kaur Ghuman: Conceptualization, Funding Acquisition, Investigation, Methodology, Project Administration, Supervision, Writing – review & editing.

## Declaration of competing interest

The authors declare the following financial interests/personal relationships, which may be considered potential competing interests: Kulbir K. Ghuman and Ana C. Tavares report that financial support was provided by the Natural Sciences and Engineering Research Council of Canada. Kulbir K. Ghuman and Ana C. Tavares report that financial support was provided by PRIMA Quebec. Kulbir K. Ghuman and Ana C. Tavares report that financial support was provided by Niobay Metals Inc. If there are other authors, they declare that they have no known competing financial interests or personal relationships that could have appeared to influence the work reported in this paper.

## References

1. G. A. Reigstad, S. Roussanaly, J. Straus, R. Anantharaman, R. de Kler, M. Akhurst, N. Sunny, W. Goldthorpe, L. Avignon and J. Pearce, *Advances in Applied Energy*, 2022, 100108.
2. S. F. Ahmed, M. Mofijur, S. Nuzhat, N. Rafa, A. Musharrat, S. S. Lam and A. Boretti, *International Journal of Hydrogen Energy*, 2021.
3. M. M. Aba, I. L. Sauer and N. B. Amado, *International Journal of Hydrogen Energy*, 2024, **57**, 660-678.
4. HYDROGEN STRATEGY FOR CANADA: Seizing the Opportunities for Hydrogen, <https://publications.gc.ca/site/eng/9.894114/publication.html>.
5. S. S. Kumar and H. Lim, *Energy reports*, 2022, **8**, 13793-13813.
6. H. Ishaq, I. Dincer and C. Crawford, *International Journal of Hydrogen Energy*, 2022, **47**, 26238-26264.
7. Z. Chen, X. Duan, W. Wei, S. Wang and B.-J. Ni, *Nano Energy*, 2020, **78**, 105392.
8. Z. P. Wu, X. F. Lu, S. Q. Zang and X. W. Lou, *Advanced Functional Materials*, 2020, **30**, 1910274.
9. K. Wang, X. Wang, Z. Li, B. Yang, M. Ling, X. Gao, J. Lu, Q. Shi, L. Lei and G. Wu, *Nano Energy*, 2020, **77**, 105162.
10. S. Kaushik, X. Xiao and Q. Xu, *EnergyChem*, 2023, **5**, 100104.
11. A. Goñi-Urtiaga, D. Presvytes and K. Scott, *International journal of hydrogen energy*, 2012, **37**, 3358-3372.
12. H. Wu, Y. Wang, Z. Shi, X. Wang, J. Yang, M. Xiao, J. Ge, W. Xing and C. Liu, *Journal of Materials Chemistry A*, 2022.
13. M. A. Hubert, L. A. King and T. F. Jaramillo, *ACS Energy Letters*, 2021, **7**, 17-23.
14. J. S. Mondschein, K. Kumar, C. F. Holder, K. Seth, H. Kim and R. E. Schaak, *Inorganic chemistry*, 2018, **57**, 6010-6015.
15. A. Liu, Z. Chen, X. Wei, W. Xiao and J. Ding, *MRS Communications*, 2017, **7**, 563-569.
16. W. Xiao, X. Huang, W. Song, Y. Yang, T. S. Herng, J. M. Xue, Y. P. Feng and J. Ding, *Nano Energy*, 2016, **25**, 60-67.
17. X. Yue, Y. Jin and P. K. Shen, *Journal of Materials Chemistry A*, 2017, **5**, 8287-8291.
18. J. C. Ruiz-Cornejo, J. F. Vivo-Vilches, D. Sebastián, M. V. Martínez-Huerta and M. J. Lázaro, *Renewable Energy*, 2021, **178**, 307-317.
19. I. Ahmed, V. Burman, R. Biswas, A. Roy, R. Sharma and K. K. Haldar, *New Journal of Chemistry*, 2023, **47**, 17284-17292.
20. Z. Wang, X. Guo, J. Montoya and J. K. Nørskov, *npj Computational Materials*, 2020, **6**, 160.
21. M. Zhao, H. Li, W. Yuan and C. M. Li, *ACS Applied Energy Materials*, 2020, **3**, 3966-3977.
22. S. Boughaba, G. Sproule, J. McCaffrey, M. Islam and M. Graham, *Thin Solid Films*, 2000, **358**, 104-113.
23. J.-H. Hur, *Computational Materials Science*, 2019, **164**, 17-21.
24. S.-H. Lee, J. Kim, S.-J. Kim, S. Kim and G.-S. Park, *Physical review letters*, 2013, **110**, 235502.
25. J. P. Perdew, K. Burke and M. Ernzerhof, *Physical review letters*, 1996, **77**, 3865.
26. S. Grimme, J. Antony, S. Ehrlich and H. Krieg, *The Journal of chemical physics*, 2010, **132**.
27. S. Grimme, S. Ehrlich and L. Goerigk, *Journal of computational chemistry*, 2011, **32**, 1456-1465.
28. L. Wang, T. Maxisch and G. Ceder, *Physical Review B*, 2006, **73**, 195107.
29. A. Jain, G. Hautier, S. P. Ong, C. J. Moore, C. C. Fischer, K. A. Persson and G. Ceder, *Physical Review B*, 2011, **84**, 045115.
30. S. Back, A. H. Bagherzadeh Mostaghimi and S. Siahrostami, *ChemCatChem*, 2022, **14**, e202101763.
31. G. Henkelman, A. Arnaldsson and H. Jónsson, *Computational Materials Science*, 2006, **36**, 354-360.
32. G. K. K. Gunasooriya and J. K. Nørskov, *ACS Energy Letters*, 2020, **5**, 3778-3787.
33. X. Miao, Z. Peng, L. Shi and S. Zhou, *ACS Catalysis*, 2023, **13**, 3983-3989.
34. P. Schütt, E. Ghasemy, A. C. Tavares and K. K. Ghuman, *ACS Applied Nano Materials*, 2023, **6**, 21829-21838.
35. S. Back, K. Tran and Z. W. Ulissi, *Acs Catalysis*, 2019, **9**, 7651-7659.
36. J. Zhang, H. B. Tao, M. Kuang, H. B. Yang, W. Cai, Q. Yan, Q. Mao and B. Liu, *Acs Catalysis*, 2020, **10**, 8597-8610.
37. J. Feng, Z. Dong, Y. Ji and Y. Li, *JACS Au*, 2023, **3**, 1131-1140.
38. J. Solla-Gullon, F. Vidal-Iglesias and J. Feliu, *Annual Reports Section "C"(Physical Chemistry)*, 2011, **107**, 263-297.
39. S. Saha, P. Gayen and V. K. Ramani, *ChemCatChem*, 2020, **12**, 4922-4929.
40. N. Soin, S. S. Roy, T. H. Lim and J. A. McLaughlin, *Materials Chemistry and Physics*, 2011, **129**, 1051-1057.
41. L. Ji, S. Yu, X. Zhou, Y. Bao, F. Yang, W. Kang and X. Zhang, *Analytica Chimica Acta*, 2019, **1079**, 86-93.



## Journal Name

## ARTICLE

42. P. Rastogi, S. Kumar, S. Bhowmick, A. Agarwal and Y. S. Chauhan, *The Journal of Physical Chemistry C*, 2014, **118**, 30309-30314.
43. N. Ma, Y. Zhang, Y. Wang, J. Zhao, B. Liang, Y. Xiong, S. Luo, C. Huang and J. Fan, *Journal of Colloid and Interface Science*, 2024, **654**, 1458-1468.
44. H. Xin, A. Vojvodic, J. Voss, J. K. Nørskov and F. Abild-Pedersen, *Physical Review B*, 2014, **89**, 115114.
45. H. Xin and S. Linic, *The Journal of chemical physics*, 2010, **132**.
46. Y. Jiao, Y. Zheng, K. Davey and S.-Z. Qiao, *Nature Energy*, 2016, **1**, 1-9.
47. I. Cohen, Y. Huang, J. Chen, J. Benesty, J. Benesty, J. Chen, Y. Huang and I. Cohen, *Noise reduction in speech processing*, 2009, 1-4.
48. L. Wang, Q. Zhou, Z. Pu, Q. Zhang, X. Mu, H. Jing, S. Liu, C. Chen and S. Mu, *Nano Energy*, 2018, **53**, 270-276.
49. Z. Fu, G. Hai, X.-X. Ma, D. Legut, Y. Zheng and X. Chen, *Journal of Energy Chemistry*, 2024, **98**, 663-669.
50. C. Yang, Y. Wu, Y. Wang, H.-N. Zhang, L.-H. Zhu and X.-C. Wang, *Nanoscale*, 2022, **14**, 187-195.
51. Y. Zhou, L. Sheng, L. Chen, W. Zhang and J. Yang, *The Journal of Physical Chemistry Letters*, 2024, **15**, 11454-11461.
52. Z. Zhang, G. Tan, A. Kumar, H. Liu, X. Yang, W. Gao, L. Bai, H. Chang, Y. Kuang and Y. Li, *Molecular Catalysis*, 2023, **535**, 112852.
53. S. Kwon, K. A. Stoerzinger, R. Rao, L. Qiao, W. A. Goddard III and Y. Shao-Horn, *Journal of the American Chemical Society*, 2024.
54. E. M. Davis, A. Bergmann, H. Kühlenbeck and B. Roldan Cuenya, *Journal of the American Chemical Society*, 2024.
55. D. Pan, Q. Liu, F. Nichols, R. Mercado, H.-L. Kuo, J. Q. Lu, F. Bridges and S. Chen, *Journal of Colloid and Interface Science*, 2023, **629**, 591-597.
56. Y. Wang, T. N. Pham, H. H. Halim, L. Yan and Y. Morikawa, *Materials Advances*, 2023, **4**, 6542-6552.

View Article Online  
DOI: 10.1039/D5LF00195A





## Data availability Statement

The structural model of Ta<sub>2</sub>O<sub>5</sub> used in this study was based on the structural coordinates from Lee, S. H., Kim, J., Kim, S. J., Kim, S., & Park, G. S. (2013), *Hidden structural order in orthorhombic Ta<sub>2</sub>O<sub>5</sub>*, *Physical Review Letters*, 110(23), 235502. (<https://doi.org/10.1103/PhysRevLett.110.235502>).

No new experimental data were generated.

